

Galaxy-scale lens search in the PEARLS NEP TDF and CEERS JWST fields

Giovanni Ferrami^{1,2*}, Nathan J. Adams³, Lewi Westcott³, Thomas Harvey³, Rolf A. Jansen⁴, Jose M. Diego⁵, Vince Estrada-Carpenter⁴, Rogier A. Windhorst^{4,6}, Christopher J. Conselice³, Anton M. Koekemoer⁷, Jordan C. J. D’Silva⁸, Christopher Willmer⁹, J. Stuart B. Wyithe^{10,2}, Michael J. Rutkowski¹¹, Seth H. Cohen⁴, Brenda L. Frye⁹, and Norman A. Grogin⁷

¹*School of Physics, University of Melbourne, Parkville, VIC 3010, Australia*

²*ARC Centre of Excellence for All-Sky Astrophysics in 3 Dimensions (ASTRO 3D), Canberra, ACT 2611*

³*Jodrell Bank Centre for Astrophysics, Alan Turing Building, University of Manchester, Oxford Road, Manchester M13 9PL, UK*

⁴*School of Earth & Space Exploration, Arizona State University, Tempe, AZ 85287-1404, USA*

⁵*Instituto de Fisica de Cantabria (CSIC-UC). Avenida. Los Castros s/n. 39005 Santander, Spain*

⁶*Department of Physics, Arizona State University, Tempe, AZ 85287-1504, USA*

⁷*Space Telescope Science Institute, 3700 San Martin Drive, Baltimore, MD 21218, USA*

⁸*International Centre for Radio Astronomy Research (ICRAR), The University of Western Australia, M468, 35 Stirling Highway, Crawley, WA 6009, Australia*

⁹*Steward Observatory, University of Arizona, 933 North Cherry Avenue, Tucson AZ, 85721, USA*

¹⁰*Research School of Astronomy and Astrophysics, Australian National University, Canberra, ACT 2611, Australia*

¹¹*Minnesota State University-Mankato, Dept. of Physics & Astronomy, Trafton Science Center North 141, Mankato, MN, 56001 USA*

Accepted XXX. Received YYY; in original form ZZZ

ABSTRACT

We present four galaxy scale lenses discovered in two JWST blank-fields: the ~ 54 arcmin² of the PEARLS North-Ecliptic-Pole Time-Domain Field (NEP TDF) and in the ~ 90 arcmin² of CEERS. We perform the search by visual inspection of NIRCcam photometric data, obtaining an initial list of 16 lens candidates. We down-select this list to 4 high-confidence lens candidates, based on lens modelling of the image configuration and photometric redshift measurements for both the source and the deflector. We compare our results to samples of lenses obtained in ground-based and space-based lens searches and theoretical expectations. We expect that JWST observations of field galaxies will yield approximately 1 galaxy scale lens every three to five NIRCcam pointings of comparable depth to these observations (~ 9 arcmin² each). This shows that JWST, compared to other lens searches, can yield an extremely high number of secure lenses per unit area, with redshift and size distributions complementary to lens samples obtained from ground-based and wide-area surveys. We estimate that a single JWST pure-parallel survey of comparable depth could yield ~ 70 galaxy scale lenses, with a third of them having $z_{\text{lens}} > 1$ and $z_{\text{source}} > 3$.

Key words: galaxies: evolution – galaxies: high-redshift – gravitational lensing: strong

1 INTRODUCTION

Strong gravitational lensing has proved to be a flexible tool to probe astrophysics and cosmology simultaneously, as it depends on the total projected mass distribution of the object acting as a lens and the cosmological distances of the lens and the background source. In particular, galaxy scale lenses can constrain the inner structure of galaxies within ~ 1 arcsecond (e.g., Treu & Koopmans 2002, Sonnenfeld et al. 2013b, Tan et al. 2024), constrain the redshift evolution of the velocity dispersion function (Kochanek 1992; Mitchell et al. 2005; Capelo & Natarajan 2007; Ferrami & Wyithe 2025), bias the observed galaxy luminosity function (e.g., Barone-Nugent et al. 2015, Mason et al. 2015, Ferrami & Wyithe 2023), measure the values of cosmological parameters from images time-delays (e.g.,

Refsdal 1964, Shajib et al. 2023) or multiple plane lenses (e.g. Collett & Auger 2014). To date, we know around $O(10^3)$ galaxy-scale lenses (many of which are only candidates that require follow-up confirmation), and therefore analyses based on samples of strong lenses have often been limited by small-number statistics.

To extract a sample of galaxy scale lenses from the photometric data, a range of lens search methods have been tested: algorithms for feature detection (e.g., More et al. 2012, Gavazzi et al. 2014) lens model fitting algorithms (e.g. Marshall et al. 2009); or a combination of the two (e.g., Sonnenfeld et al. 2018); visual search by researchers (Hogg et al. 1996; Moustakas et al. 2007; Faure et al. 2008; Nightingale et al. 2025); citizen science (Marshall et al. 2016; More et al. 2016; Sonnenfeld et al. 2020). In addition, various machine learning architectures have been employed so far in lens searches Convolutional Neural Networks (CNNs, see for example Jacobs et al. 2019, Euclid Collaboration et al. 2024), Support Vector Machines (SVM,

* E-mail: gferrami@student.unimelb.edu.au

e.g., [Hartley et al. 2017](#)) and self-attention encoding (e.g., [Thuruthipilly et al. 2022](#)).

The degree of completeness and purity of a particular lens search method when applied to real data is hard to reliably estimate, and visual inspection can outperform other forms of automated search, such as neural networks (e.g., [Holloway et al. 2024](#), which also shows that combining visual inspection with CNNs can improve the final sample).

By the end of this decade, wide-field photometric surveys are expected to yield $\mathcal{O}(10^5)$ strong lenses, two orders of magnitude more than the current sample ([Collett 2015](#), [Holloway et al. 2023a](#), [Ferrami & Wyithe 2024](#)). These surveys include the Euclid Wide survey ([Euclid Collaboration et al. 2022](#)), Vera Rubin Observatory LSST ([Ivezic et al. 2008](#)), and Roman Space Telescope High Latitude Wide Area Survey ([Spergel et al. 2015](#)). Compared to these large surveys, a typical field observed by James Webb Space Telescope (JWST) photometry is smaller, but much deeper in flux, with much better spatial resolution, and with several near-infrared (NIR) filters that can see faint red sources behind bright deflectors. These characteristics allow JWST to probe a different regime of lenses, both in redshift and angular size.

In this article, we report on a visual search of galaxy scale lenses in two JWST fields of comparable size, PEARLS North Ecliptic Pole Time Domain Field (NEP TDF) 54 arcmin² and CEERS ~ 90 arcmin², both with ancillary Hubble Space Telescope (HST) optical photometry to enable accurate photometric redshift estimation. We find 6 candidates, divided equally between the two fields at lower angular sizes and higher redshifts than lens samples identified by ground-based and optical surveys, in agreement with theoretical expectations, and with recent findings of the COWLS lens search, conducted in the COSMOS-Web field ([Nightingale et al. 2025](#); [Mahler et al. 2025](#); [Hogg et al. 2025](#)).

This article is structured as follows. In Section 2 we describe the reduction of the photometry of the two fields. In Section 3 we introduce the strategy for visual inspection, SED fitting and lens modelling. In Section 4 we present the results of the lens search and discuss how the resulting distributions compare with previous surveys and theoretical expectations. Finally, in Section 5 we present our conclusions.

Throughout this paper, we adopt $H_0 = 70 \text{ km s}^{-1} \text{ Mpc}^{-1}$, $\Omega_0 = 0.3$, $\Omega_\Lambda = 0.7$.

2 DATA

In this paper we used publicly available HST and JWST data drawn from the Prime Extragalactic Areas for Reionization and Lensing Science (PEARLS, PIs: R. Windhorst & H. Hammel, PIDs: 1176 & 2738, [Windhorst et al. 2023](#)) North Ecliptic Pole Time-Domain Field (NEP TDF; [Jansen & Windhorst 2018](#)) and the Cosmic Evolution Early Release Science (CEERS, PID: 1345, PI: S. Finkelstein, [Finkelstein et al. 2023](#); [Bagley et al. 2023](#)) programs. These two fields were chosen because both:

- are blank-fields (i.e., not centred on a cluster), allowing us to study the galaxy-scale strong lensing statistics,
- have footprints smaller than $\sim 100 \text{ arcmin}^2$, with deeper photometry to detect the faint light of lensed background sources over a large range of redshifts,
- contain at least 9 photometric filters from JWST/NIRCam and HST/ACS combined, to enable robust SED fitting.

2.1 PEARLS NEP Time-Domain Field

This field is located within JWSTs continuous viewing zone, meaning it is accessible to JWST and HST at any time of the year. The PEARLS data consists of 8 partially overlapping NIRCam pointings that are grouped into 4 pairs. Each pair of pointings is taken 3 months apart, resulting in a cross/windmill shaped geometry for the field. NIRCam data were reduced as part of the EPOCHS project, using JWST pipeline version 1.8.2, calibration pmap1084 and a pixel scale of 0.03as/pix ([Adams et al. 2024](#); [Conselice et al. 2025](#)). In addition to standard calibrations, we employ the use of a 1/f correction developed by Chris Willott¹ and subtract scaled templates of ‘Wisp’ artefacts in the F150W and F200W images. There are a total of 8 NIRCam bands spanning ~ 60 square arcmins, including F090W, F115W, F150W, F200W, F277W, F356W, F410M, F444W. We calculate point-source depths ranging from 28.5-29.3 within 0.32as diameter apertures ($\sim 80\%$ enclosed PSF flux) from the random scattering of empty apertures across the final mosaic. Part of this field is also covered by NIRISS slitless spectroscopy ([Estrada-Carpenter et al. \[in prep.\]](#)). While in this work we focus on the photometric redshift obtained from the SED fitting over the available filters, the NIRISS spectra of one of the lenses found in our sample (PEARLS172239+655143) is analysed in [Adams et al. \(2025\)](#).

To aid photometric analysis, we include HST imaging in the F606W filter from the TREASUREHUNT programme ([O’Brien et al. 2024](#), [Jansen et al. in prep.](#), GO 15278, PI: R. Jansen and GO 16252/16793, PIs: R. Jansen & N. Grogin), pixel matched to the JWST imaging. Data spans from Oct 2017 to Oct 2022 and provides F275W, F435W and F606W ACS imaging over 194 square arcminutes. The F606W mosaic has a comparable depth to the JWST data, with a limiting 5σ magnitude of 28.5 in the same aperture size of 0.32as, whilst the bluer bands are upwards of 1 magnitude shallower. For this reason, we only employ the use of the F606W mosaic in this study. Details of HST data reduction, as well as the general field/survey geometry, are provided in [O’Brien et al. \(2024\)](#).

2.2 CEERS

This study also makes use of both primary observing runs (July 2022 & December 2022) of the CEERS survey. This consists of 10 NIRCam pointings mosaiced over the Extended Groth Strip (EGS; [Groth et al. 1994](#)) with 7 photometric bands (F115W, F150W, F200W, F277W, F356W, F410M and F444W). We use the mosaics produced using the same pipeline as our NEP-TDF images described above. This field provides the a contiguous area of 64.15 square arcminutes after masking and it reaches depths between apparent magnitudes of 28.6 and 29.3. The field does lack the F090W band and so we include HST CANDELS imaging of the F606W and F814W filters that was reduced by the CEERS team (their HDR1) following [Koekemoer et al. \(2011\)](#) in order to cover this bluer wavelength range.

3 IDENTIFYING THE LENS SAMPLE

The process we followed to identify the 4 lenses presented in this work started with a visual inspection of the PEARLS NEP-TDF and CEERS fields, which yielded an initial set of 16 candidate lenses (see Appendix and Figure A1). Classifying a candidate as a genuine lens requires that the geometry of the system is compatible

¹ <https://github.com/chriswillott/jwst/tree/master>

with a lensing system (i.e. the deflector and the source lie at different redshifts, to be confirmed spectroscopically), and a model for the total projected mass and source light that could reproduce the observed strong lensing features. One of our candidate systems, PEARLS172239+655143, is located within the NIRISS F200W field of view. A detailed analysis of this system, including its spectra, can be found in [Adams et al. \(2025\)](#). In this paper, we relied on photometric redshifts of both deflector and source of each candidate and we fitted the available photometry to a parametric lens model. These steps lead us to final list of 4 high-confidence lens candidates, shown in Figure 1. The visual inspection step, the SED fitting procedure (necessary to obtain the redshift estimates), and lens fitting process are described in the following subsections.

3.1 Visual Inspection

Since the total area obtained combining the PEARLS NEP-TDF and CEERS fields is around 144 arcmin^2 , we were able to conduct a visual inspection of the whole field, without restricting the search around massive galaxies (i.e., without introducing luminosity cuts to the deflector population). Visual inspection was conducted by GF, RAJ, and JMD in the NEP-TDF, and by GF in CEERS. The inspectors looked at the coloured images of all JWST pointings constructed by mapping the light intensity observed in the F444W, F277W, and F150W bands for the red, green, and blue channels, respectively. Each field was inspected twice to obtain an initial list of 16 candidates that showed some morphological feature that looked possibly due to strong lensing. Half of these candidates lie in the NEP-TDF field and half in CEERS.

3.2 SED modelling and photometric redshift

We model the foreground elliptical of each initial candidate by providing PSF homogenised images to the `galfit` code ([Peng et al. 2010](#)). PSF homogenisation was conducted with the use of `pypher` ([Boucaud, A. et al. 2016](#)) and model PSFs are generated following an empirical approach for both the JWST and HST imaging ([Skelton et al. 2014](#); [Whitaker et al. 2019](#); [Weaver et al. 2024](#)). We use the underlying image weight maps to identify and cut out a large region around our source which uses the same combination of mosaiced images to produce our empirical PSF model. To account for this, and following the methods and work in [Westcott et al. \(2025\)](#), single and double Sérsic profiles are fit to the elliptical galaxy with surrounding sources masked in each photometric band. Using this method we find that a single Sérsic profile fits the source well. To obtain an initial photometric redshift for the foreground galaxy, we provide the SED fitting code `EAZY` ([Brammer et al. 2008](#)) with aperture photometry extracted from the light profile fit using the base set of FSPS models. For the higher- z background galaxy, we trial the use of both default FSPS models in `EAZY` ([Conroy et al. 2009](#); [Conroy & Gunn 2010](#)) in addition to templated featuring bluer SEDs and stronger emission lines derived in the work by ([Larson et al. 2023](#)) and obtain similar redshifts. For the process of obtaining an initial photo- z estimate, photometric errors are fixed to 10%. For stellar masses, fluxes extracted within circular apertures of radius θ_E are run through the SED fitting tool `BAGPIPES` ([Carnall et al. 2018](#)) using a fiducial Kroupa IMF and the same set up as ([Harvey et al. 2025](#)). To summarise here; we use `LogNormal` star formation histories and fix the redshift to the spec- z if available or use a prior following a Gaussian approximation of the `EAZY` $P(z)$ otherwise. [Calzetti et al. \(2000\)](#) dust extinction up to 3.5 mags is allowed and broad, uniform priors on other parameters such as metallicity.

3.3 Lens modelling

To confirm that the observed image configuration is compatible with strong lensing, we model each system with a simple parametric model. We model the deflector as a Singular Isothermal Ellipsoid (SIE) mass distribution with external shear, and the deflector and background source light as an elliptical Sérsic profile ([Sersic 1968](#)). The total mass distribution within the Einstein radius of early-type galaxies (ETGs) is well approximated by an isothermal distribution, such as the SIE (e.g. [Gavazzi et al. 2007](#), [Koopmans et al. 2009](#), [Lapi et al. 2012](#), [Sonnenfeld 2024](#)). The external shear component accounts for additional shear introduced by line-of-sight perturbers and compensate for the simplicity in the angular structure of the main deflector model (e.g. [Etherington et al. 2024](#)). To perform the parametric lens fitting we use the `lens` astronomy package ([Birrer & Amara 2018](#); [Birrer et al. 2021](#)). In the fitting process, we introduce an appropriately sized annular mask to avoid large residuals in the centre of the lens light profile (within $\approx 0.3''$, where the Sérsic profile is less adequate in reproducing the observations), and block out the light from the line-of-sight galaxies in the outer region. We sampled from the posterior probability distribution function (PDF) of the model parameters with the Markov chain Monte Carlo (MCMC) affine invariant method ([Goodman & Weare 2010](#)) using `emcee` ([Foreman-Mackey et al. 2013](#)). To achieve faster convergence in the MCMC sampling, we choose the initial points of the Markov-chain from the best-fitting parameters obtained with the particle swarm optimization (PSO) method ([Kennedy & Eberhart 1995](#)). The SED and lens modelling yielded 4 high-confidence lens candidates, shown in Figure 1, with their the lens models shown in Figure 2.

4 RESULTS OF THE LENS SEARCH

The position and redshift of the final sample of 4 lenses are summarised in Table 1, and the parameters of the best fitting lens model and stellar mass are listed in Table 2. The lens redshift and source redshift ranges are $0.38 < z_{\text{lens}} < 1.25$ and $1 < z_{\text{source}} < 3.6$, respectively. Their Einstein radii range between $0.7'' < \theta_E < 1.3''$, and the velocity dispersion entering the SIE model ranges between $200 < \sigma / (\text{km/s}) < 250$, consistent with the predictions of the fiducial model in [Ferrami & Wyithe \(2024\)](#). The NEP TDF field lens PEARLS172239+655143 has a photo- z for the background source of ~ 3.6 , amongst the highest in known galaxy-scale deflectors. A more detailed analysis of this system can be found in [Adams et al. \(2025\)](#).

After having identified the 4 high confidence lenses in our sample, we cross checked previous lens searches and found that CEERS142032+525823 was also found in the SL2S lens search ([Sonnenfeld et al. 2013a,b](#)) (identified there as SL2SJ142031+525822 and classified as grade B, potential lens). We choose to use the spectroscopic redshifts for deflector and source presented in SL2S in Table 1, also because this lens falls partially in the gap of the bluest NIRCcam filter available.

The projected stellar and total mass estimates, obtained from `BAGPIPES` and the best fitting lens model respectively, are presented in Table 3. The range of stellar-to-total mass ratio in our sample is consistent with the dark matter fraction found in other sample of lenses (e.g. in SL2S, [Sonnenfeld et al. 2015](#)). We do not explore the contribution of different choices of IMF on the inferred mass ratios as our sample is limited to photometric redshifts, which could bias the total projected mass (e.g. [Shuntov et al. 2025](#)).

In Figure 3 we compare the distributions in lens and source redshifts, and Einstein radius found in our sample to the Strong Lensing

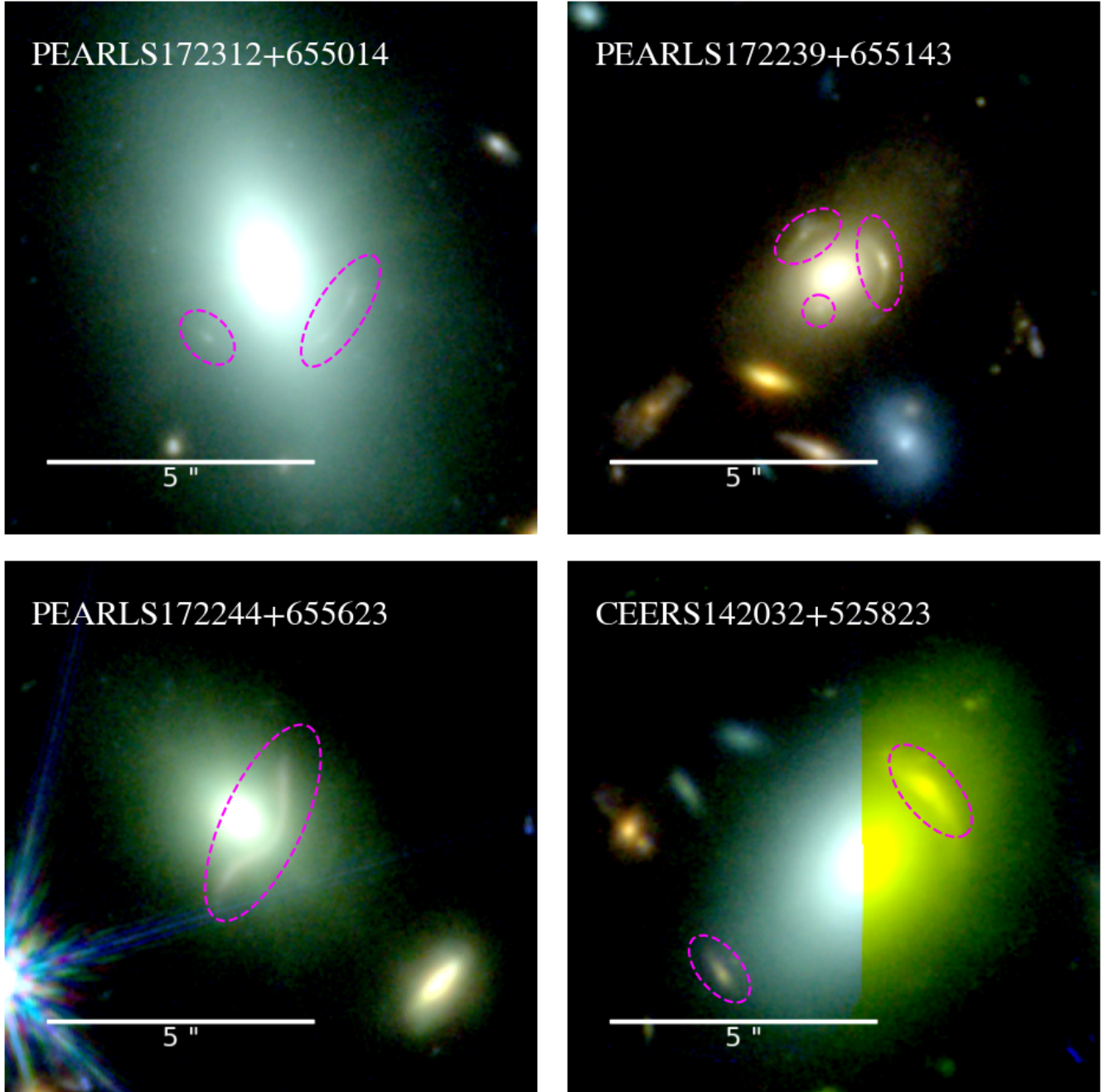


Figure 1. Lens candidates in PEARLS NEP field and CEERS fields. The cutouts are $10'' \times 10''$, and the magenta contours highlight the potential lensing features noticed in the visual inspection process. We note that the main arc in CEERS142032+525823 lies in the region where there is no blue NIRCam data.

Legacy Survey (SL2S, Cabanac et al. 2007), which is based on an algorithmic lens search in the Canada–France–Hawaii Telescope Legacy Survey (CFHTLS) with follow-up ground based spectroscopy, and the COSMOS-Web Lens Survey (COWLS, Nightingale et al. 2025), which consists in a visual inspection of the COSMOS-Web JWST field. Figure 4 shows the link between the lens redshift and Einstein radius distributions for the three surveys introduced before, where the contours are calculated using *galess*² (Ferrami & Wyithe 2024).

² <https://github.com/Ferr013/GALESS>

This shows that a lens search conducted on JWST photometry can probe higher redshift of the lens and lower Einstein radii sized compared to ground based surveys. We note that the distributions observed in the COWLS sample might be explained by imposing an upper bound in velocity dispersion (i.e. total mass) of the lens. The cut in velocity dispersion was estimated using the $M_{\star} - \sigma$ relation from Cannarozzo et al. (2020), noticing that the stellar masses in the COWLS lens sample are nearly all below $\log(M_{\star}/M_{\odot}) = 11$ and have mean deflector redshift ≈ 0.95 . If we apply this cut in velocity dispersion to the expectations for the SL2S sample (shaded dashed

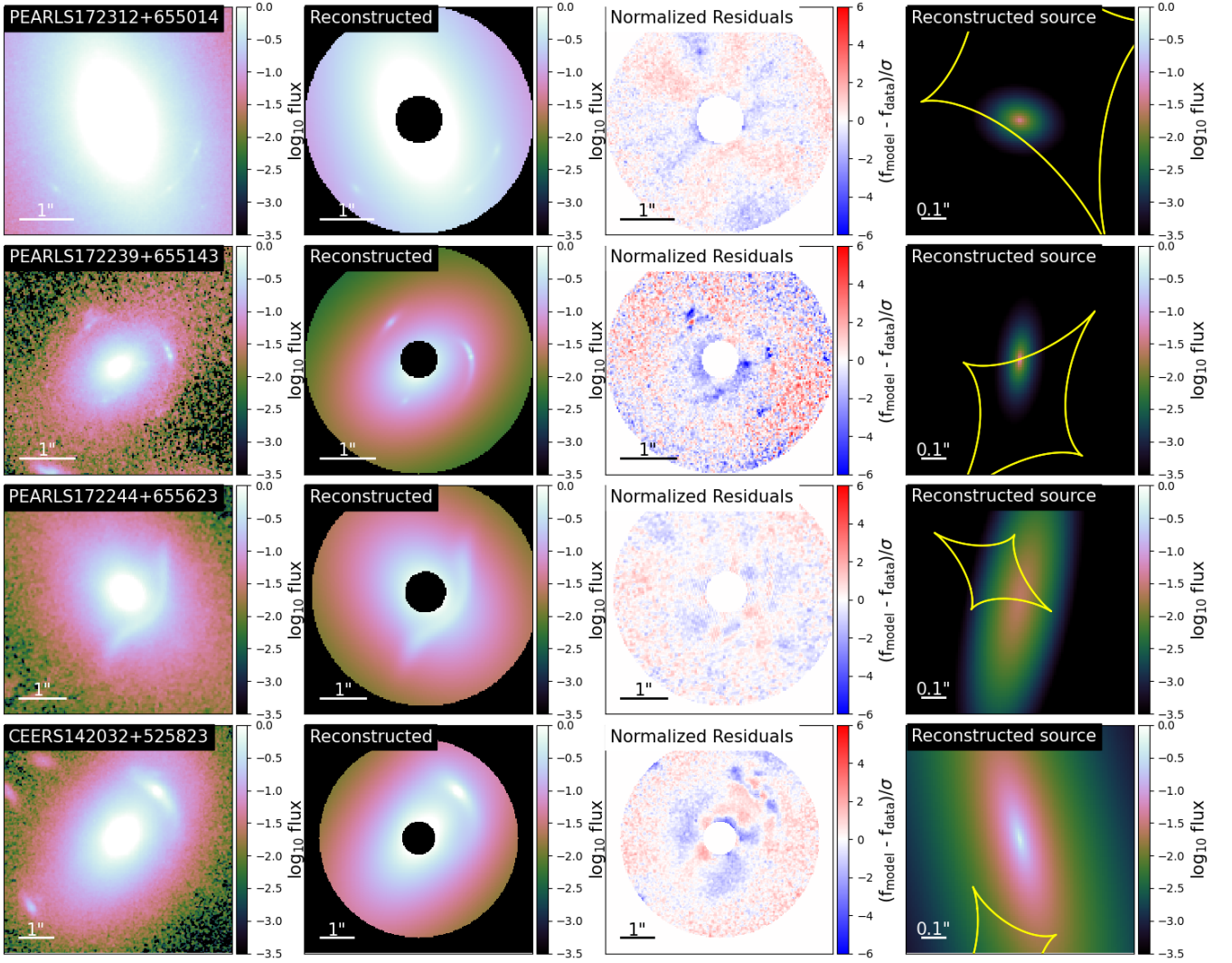


Figure 2. The four lenses fit with a SIE mass distribution plus external shear. From left to right, the panels show the single-band image data (F444W) for each lens, our reconstruction of the image, the residual difference between the image and the reconstructed source plane, with the tangential caustic highlighted in yellow.

contours), we are constrained to a parameter space region smaller than the available observations. We consider also the correlation between lens and source redshifts in Figure 5. It is clear that JWST will be able to probe much deeper redshifts compared to ground based surveys (also considering the limits in determining emission lines with near-infrared spectroscopy imposed by the earth atmosphere, which are accounted for in the calculation for the probability contours in SL2S).

When compared to other lens searches, our sample yields an extremely high number of secure lenses per unit area. Accounting for $\sim 30\%$ of cosmic variance (Trenti & Stiavelli 2008, calculated considering the fact that our total area, obtained combining PEARLS NEP TDF and CEERS, is non contiguous), the number of high-confidence candidates in our sample leads to a density of 100 ± 30 galaxy scale lenses per square degree, equivalent to a strong lens candidate every three to five NIRCcam pointings (9 arcmin² each). These number are lower bounds depending on the completeness of our search. These densities are compatible with the theoretical predictions of Holloway et al. (2023b) and Ferrami & Wyithe (2024).

As a comparison, the SL2S lens search yielded 36 secure lenses over 170 deg², while the search conducted in DES by Jacobs et al. (2019) yielded 500 candidates over 5000 deg² (of which 138 are spectroscopically confirmed, Barone et al. 2025). The recent lens search conducted in the COSMOS-Web JWST field yielded 17 secure lenses over an area of 0.54 deg² (Nightingale et al. 2025), with about 400 more with varying degrees of confidence. Our results suggest that there should be slightly less than a hundred true positive amongst the COWLS candidates, as discussed in Hogg et al. (2025).

5 DISCUSSION AND CONCLUSIONS

We performed a search for galaxy-scale strong lenses in 144 arcmin² of JWST NIRCcam data, combining the PEARLS NEP TDF and CEERS fields, each containing observations in 9 photometric filters down to mag 28.5. We first visually inspected each NIRCcam pointing, isolating 16 lens candidates, which we subsequently tested for having different redshift between deflector and source with SED

Table 1. Catalogue of the lens candidates presented in this work.

Name	R.A.	DEC	$z_{\text{lens}}^{\text{phot}}$	$z_{\text{source}}^{\text{phot}}$
(1)	(2)	(3)	(4)	(5)
PEARLS172312+655014	17:23:11.93	+65:50:14.32	$^{\dagger}0.3741^{+0.0002}_{-0.0002}$	$2.35^{+0.05}_{-0.15}$
PEARLS172239+655143	17:22:38.98	+65:51:43.16	$1.25^{+0.25}_{-0.25}$	$3.60^{+0.10}_{-0.10}$
PEARLS172244+655623	17:22:43.90	+65:56:22.97	$0.60^{+0.09}_{-0.11}$	$1.45^{+0.14}_{-0.21}$
CEERS142032+525823	14:20:31.80	+52:58:22.90	$^{\ddagger}0.380^{+0.005}_{-0.005}$	$0.99^{+0.05}_{-0.05}$

Notes. The columns indicate the (1) lens name, (2) right ascension and (3) declination, (4) photometric redshifts of the deflector and (5) of the background source. *Comments.* † This deflector has spectroscopic redshift measured with Binospec at the MMT [Willmer, personal communication]. ‡ This system was also identified as a probable lens (grade B) in SL2S (Sonnenfeld et al. 2013b), with the measured spectroscopic redshifts reported in the table. Our estimate of the photo-z for this galaxies has a large error due to NIRCcam blue module gap: $z_{\text{lens}}^{\text{phot}} = 0.1^{+0.4}_{-0.05}$, $z_{\text{source}}^{\text{phot}} = 0.75^{+0.63}_{-0.33}$.

Table 2. Lens model parameters and stellar mass for the 4 best lens candidates.

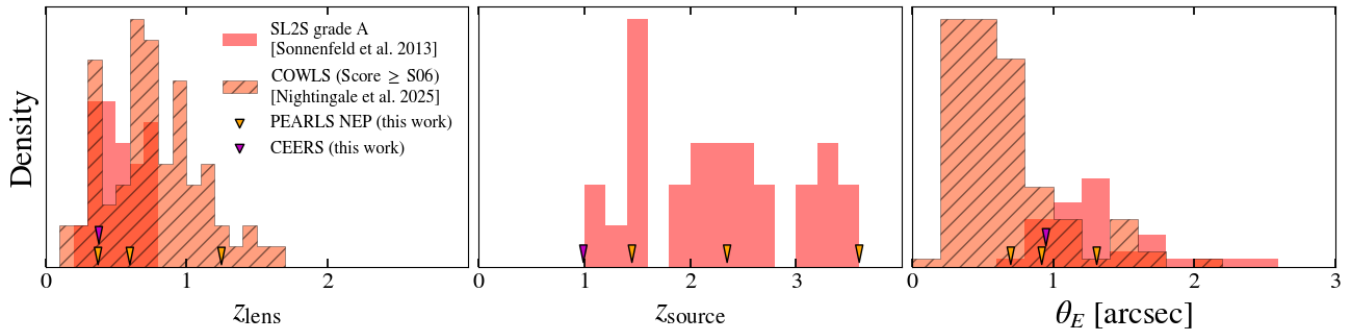
Name	θ_E ["]	q	P.A. [°]	γ_1	γ_2	σ^{SIE} [km s $^{-1}$]
(1)	(2)	(3)	(4)	(5)	(6)	(7)
PEARLS172312+655014	$1.31^{+0.09}_{-0.08}$	$0.51^{+0.02}_{-0.05}$	$-73.9^{+10.2}_{-12.4}$	$0.02^{+0.02}_{-0.01}$	$0.05^{+0.04}_{-0.02}$	225^{+14}_{-33}
PEARLS172239+655143	$0.92^{+0.02}_{-0.01}$	$0.38^{+0.01}_{-0.01}$	$46.4^{+0.8}_{-1.9}$	$0.04^{+0.02}_{-0.01}$	$0.10^{+0.01}_{-0.01}$	247^{+6}_{-5}
PEARLS172244+655623	$0.70^{+0.01}_{-0.01}$	$0.79^{+0.02}_{-0.02}$	$42.8^{+1.9}_{-4.2}$	$-0.07^{+0.01}_{-0.01}$	$0.23^{+0.01}_{-0.01}$	204^{+35}_{-20}
CEERS142032+525823	$0.95^{+0.01}_{-0.01}$	$0.53^{+0.01}_{-0.01}$	$38.4^{+0.3}_{-0.4}$	$0.29^{+0.01}_{-0.01}$	$0.15^{+0.01}_{-0.01}$	223^{+9}_{-17}

Notes. The columns indicate the (1) lens name; (2) Einstein radius in arcseconds, (3) lens axis ratio and (4) position angle; the (5)(6) external shear components; and (7) deflector velocity dispersion entering the isothermal mass profile, in km/s.

Table 3. Total and stellar mass within the Einstein radius.

Name	θ_E [kpc]	$\log M_{\text{tot}, \leq \theta_E} / M_{\odot}$	$\log M_{\star, \leq \theta_E}^{\text{Kroupa}} / M_{\odot}$	$(M_{\star} / M_{\text{tot}})_{\leq \theta_E}$
(1)	(2)	(3)	(4)	(5)
PEARLS172312+655014	$7.27^{+0.01}_{-0.41}$	$11.54^{+0.06}_{-0.05}$	$11.31^{+0.17}_{-0.17}$	$0.58^{+0.39}_{-0.24}$
PEARLS172239+655143	$7.67^{+0.01}_{-0.38}$	$11.61^{+0.10}_{-0.11}$	$11.11^{+0.07}_{-0.08}$	$0.31^{+0.16}_{-0.11}$
PEARLS172244+655623	$4.68^{+0.01}_{-0.51}$	$11.23^{+0.17}_{-0.14}$	$10.59^{+0.12}_{-0.12}$	$0.23^{+0.19}_{-0.11}$
CEERS142032+525823	$4.95^{+0.01}_{-0.34}$	$11.34^{+0.06}_{-0.07}$	$10.45^{+0.12}_{-0.20}$	$0.13^{+0.07}_{-0.06}$

Notes. The columns indicate the (1) lens name; the (2) Einstein radius in kpc; the (3) total projected mass and the (4) projected stellar mass within the Einstein radius; and (5) the stellar-to-total mass ratio.

**Figure 3.** Properties of our lens sample (arrows) compared with the lenses in SL2S (red, Sonnenfeld et al. 2013b) and COWLS (orange dashed, Nightingale et al. 2025). The left and middle panels show the deflector and source redshift distributions, respectively. The right panel shows the Einstein radius distribution.

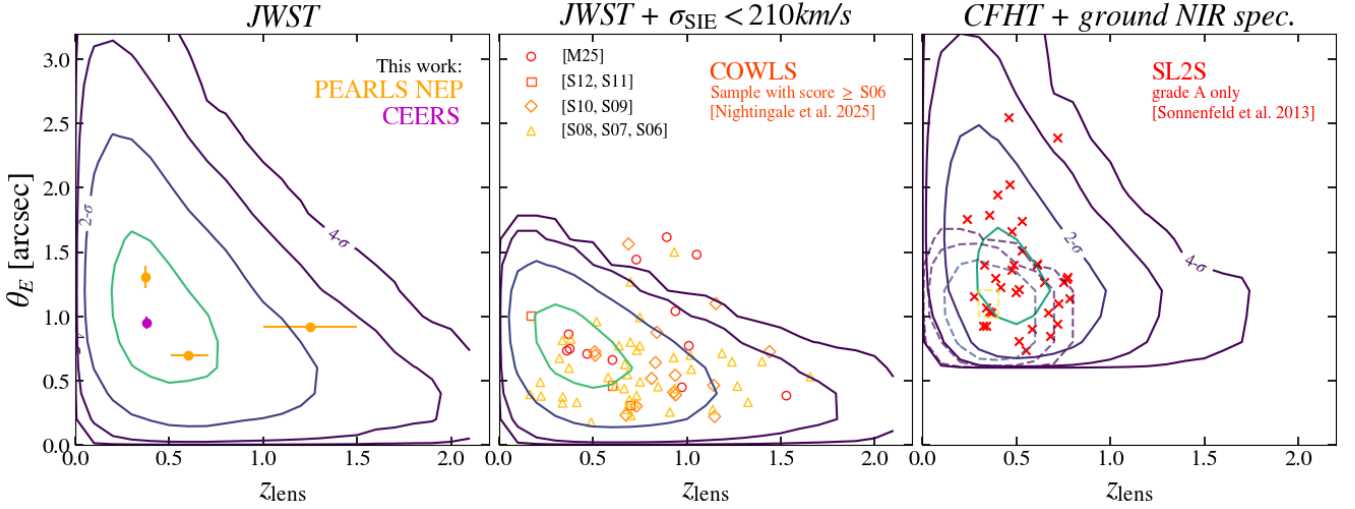


Figure 4. Comparison between the Einstein radius vs lens redshift distribution in our sample of lenses (left panel, orange and purple points), in COWLS (central panel, markers are mapped to the confidence score of each lens, S06 being the lowest and M25 the highest) and SL2S (right panel, red crosses). On top of each panel is reported the telescope used to conduct the relative lens search. The contours represent the iso-probability levels predicted using the `galens` analytical model (Ferrami & Wyithe 2024), including a cut in velocity dispersion ($\sigma_{\text{SIE}} < 210 \text{ km/s}$) in the central panel. The shaded dashed contours in the right panel represent the expected distribution in SL2S if we assume the cut in velocity dispersion required to reproduce the distribution of COWLS.

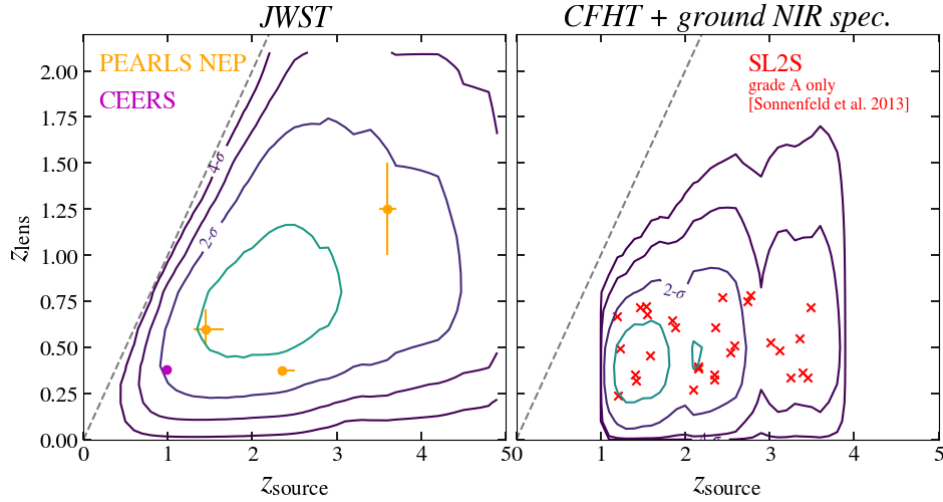


Figure 5. Deflector vs source redshift distribution in our sample (left) and SL2S (right), presented as in Figure 4.

modelling, and for having image configurations compatible with a SIE mass distribution plus external shear. After applying these restrictions, we obtain a sample of 4 lenses, corresponding to a density of 100 ± 30 lenses per deg^2 . We study the redshift and angular size distributions of this sample, comparing it with past searches and theoretical expectations. We confirm that a large fraction of the lenses discoverable by JWST ($\sim 30\%$) will be above redshift $z_{\text{lens}} > 1$ and have magnified sources with $z_{\text{source}} > 3$, such as PEARLS172239+655143 or the COSMOS-Web Ring (Mercier et al. 2024; van Dokkum et al. 2024; Shuntov et al. 2025), and most Einstein radii smaller than 1". Given the results of this article, we expect ~ 25 of these high- z lenses in COWLS (Nightingale et al. 2025) or a single Pure Parallel program (equivalent to around 200 NIRCcam pointings). Such a set of high redshift lenses can be used to constrain the evolution of the elliptical galaxies mass function at redshift range

higher than what is available now. A sample of lensing systems with high redshifts and small angular sizes can also be used to train neural network lens finders on a range of parameters that has not been explored so far.

ACKNOWLEDGMENTS

G.F and J.S.B.W. acknowledge the support of the Australian Research Council Centre of Excellence for All Sky Astrophysics in 3 Dimensions (ASTRO 3D), through project number CE170100013, and the We acknowledge support from the ERC Advanced Investigator Grant EPOCHS (788113), as well as two studentships from STFC. J.M.D. acknowledges support from project PID2022-138896NB-C51 (MCIU/AEI/MINECO/FEDER, UE) Ministerio de

Ciencia, Investigación y Universidades. This work is based on observations made with the NASA/ESA Hubble Space Telescope (HST) and NASA/ESA/CSA James Webb Space Telescope (JWST) obtained from the Mikulski Archive for Space Telescopes (MAST) at the Space Telescope Science Institute (STScI), which is operated by the Association of Universities for Research in Astronomy, Inc., under NASA contract NAS 5-03127 for JWST, and NAS 5–26555 for HST. The observations used in this work are associated with JWST programme 2738 and raw images are available on the MAST archive. The authors thank all involved in the construction and operations of the telescope as well as those who designed and executed these observations, their number are too large to list here and without each of their continued efforts, such work would not be possible.

SOFTWARE

This work used the following software packages: *astropy* (Astropy Collaboration et al. 2013), *pypher* (Boucaud, A. et al. 2016), *galfit* (Peng et al. 2010), *EAZY* (Brammer et al. 2008), *BAGPIPES* (Carnall et al. 2018), *lenstronomy* (Birrer & Amara 2018; Birrer et al. 2021), *galoss* (Ferrami & Wyithe 2024), *NumPy* (Harris et al. 2020), *Matplotlib* (Hunter 2007), *SciPy* (Virtanen et al. 2020).

DATA AVAILABILITY

JWST data from PEARLS programme ID 2738 is publicly available on the MAST portal and accessible at [this link](#). Accompanying HST data from TREASUREHUNT is available from <https://doi.org/10.17909/wv13-qc14>. JWST data from CEERS is publicly available at <https://ceers.github.io/dr07.html>.

REFERENCES

- Adams N. J., et al., 2024, *ApJ*, 965, 169
 Adams N. J., et al., 2025, *arXiv e-prints*, p. [arXiv:2504.03571](#)
 Astropy Collaboration et al., 2013, *A&A*, 558, A33
 Bagley M. B., et al., 2023, *ApJ*, 946, L12
 Barone-Nugent R. L., Wyithe J. S. B., Trenti M., Treu T., Oesch P., Bouwens R., Illingworth G. D., Schmidt K. B., 2015, *MNRAS*, 450, 1224
 Barone T. M., et al., 2025, *arXiv e-prints*, p. [arXiv:2503.08041](#)
 Birrer S., Amara A., 2018, *Physics of the Dark Universe*, 22, 189
 Birrer S., et al., 2021, *Journal of Open Source Software*, 6, 3283
 Boucaud, A. Bocchio, M. Abergel, A. Orioux, F. Dole, H. Hadj-Youcef, M. A. 2016, *A&A*, 596, A63
 Brammer G. B., van Dokkum P. G., Coppi P., 2008, *ApJ*, 686, 1503
 Cabanac R. A., et al., 2007, *A&A*, 461, 813
 Calzetti D., Armus L., Bohlin R. C., Kinney A. L., Koornneef J., Storchi-Bergmann T., 2000, *ApJ*, 533, 682
 Cannarozzo C., Sonnenfeld A., Nipoti C., 2020, *MNRAS*, 498, 1101
 Capelo P. R., Natarajan P., 2007, *New Journal of Physics*, 9, 445
 Carnall A. C., McLure R. J., Dunlop J. S., Davé R., 2018, *MNRAS*, 480, 4379
 Collett T. E., 2015, *ApJ*, 811, 20
 Collett T. E., Auger M. W., 2014, *MNRAS*, 443, 969
 Conroy C., Gunn J. E., 2010, *ApJ*, 712, 833
 Conroy C., Gunn J. E., White M., 2009, *ApJ*, 699, 486
 Conselice C. J., et al., 2025, *ApJ*, 983, 30
 Estrada-Carpenter V., et al., 2024, *MNRAS*, 532, 577
 Etherington A., et al., 2024, *MNRAS*, 531, 3684
 Euclid Collaboration et al., 2022, *A&A*, 662, A112
 Euclid Collaboration et al., 2024, *A&A*, 681, A68
 Faure C., et al., 2008, *ApJS*, 176, 19
 Ferrami G., Wyithe J. S. B., 2023, *MNRAS*, 523, L21
 Ferrami G., Wyithe J. S. B., 2024, *MNRAS*, 532, 1832
 Ferrami G., Wyithe J. S. B., 2025, *MNRAS*, 537, 779
 Finkelstein S. L., et al., 2023, *ApJ*, 946, L13
 Foreman-Mackey D., Hogg D. W., Lang D., Goodman J., 2013, *PASP*, 125, 306
 Gavazzi R., Treu T., Rhodes J. D., Koopmans L. V. E., Bolton A. S., Burles S., Massey R. J., Moustakas L. A., 2007, *ApJ*, 667, 176
 Gavazzi R., Marshall P. J., Treu T., Sonnenfeld A., 2014, *ApJ*, 785, 144
 Goodman J., Weare J., 2010, *Communications in Applied Mathematics and Computational Science*, 5, 65
 Groth E. J., Kristian J. A., Lynds R., O’Neil Jr. E. J., Balsano R., Rhodes J., WFPC-1 IDT 1994, in *American Astronomical Society Meeting Abstracts*. p. 53.09
 Harris C. R., et al., 2020, *Nature*, 585, 357
 Hartley P., Flamary R., Jackson N., Tagore A. S., Metcalf R. B., 2017, *MNRAS*, 471, 3378
 Harvey T., et al., 2025, *ApJ*, 978, 89
 Hogg D. W., Blandford R., Kundic T., Fassnacht C. D., Malhotra S., 1996, *ApJ*, 467, L73
 Hogg N. B., et al., 2025, *arXiv e-prints*, p. [arXiv:2503.08785](#)
 Holloway P., Verma A., Marshall P. J., More A., Tecza M., 2023a, *MNRAS*, 525, 2341
 Holloway P., Verma A., Marshall P. J., More A., Tecza M., 2023b, *MNRAS*, 525, 2341
 Holloway P., Marshall P. J., Verma A., More A., Cañameras R., Jaelani A. T., Ishida Y., Wong K. C., 2024, *MNRAS*, 530, 1297
 Hunter J. D., 2007, *Computing in Science & Engineering*, 9, 90
 Ivezić Z., et al., 2008, *Serbian Astronomical Journal*, 176, 1
 Jacobs C., et al., 2019, *MNRAS*, 484, 5330
 Jansen R. A., Windhorst R. A., 2018, *PASP*, 130, 124001
 Kennedy J., Eberhart R., 1995, in *Proceedings of ICNN’95 - International Conference on Neural Networks*. pp 1942–1948 vol.4, [doi:10.1109/ICNN.1995.488968](#)
 Kochanek C. S., 1992, *ApJ*, 384, 1
 Koekemoer A. M., et al., 2011, *ApJS*, 197, 36
 Koopmans L. V. E., et al., 2009, *ApJ*, 703, L51
 Lapi A., Negrello M., González-Nuevo J., Cai Z. Y., De Zotti G., Danese L., 2012, *ApJ*, 755, 46
 Larson R. L., et al., 2023, *ApJ*, 958, 141
 Mahler G., et al., 2025, *arXiv e-prints*, p. [arXiv:2503.08782](#)
 Marshall P. J., Hogg D. W., Moustakas L. A., Fassnacht C. D., Bradač M., Schrabback T., Blandford R. D., 2009, *ApJ*, 694, 924
 Marshall P. J., et al., 2016, *MNRAS*, 455, 1171
 Mason C. A., et al., 2015, *ApJ*, 805, 79
 Mercier W., et al., 2024, *A&A*, 687, A61
 Mitchell J. L., Keeton C. R., Frieman J. A., Sheth R. K., 2005, *ApJ*, 622, 81
 More A., Cabanac R., More S., Alard C., Limousin M., Kneib J. P., Gavazzi R., Motta V., 2012, *ApJ*, 749, 38
 More A., et al., 2016, *MNRAS*, 455, 1191
 Moustakas L. A., et al., 2007, *ApJ*, 660, L31
 Nightingale J., et al., 2025, *arXiv e-prints*, p. [arXiv:2503.08777](#)
 O’Brien R., et al., 2024, *ApJS*, 272, 19
 Peng C. Y., Ho L. C., Impey C. D., Rix H.-W., 2010, *AJ*, 139, 2097
 Refsdal S., 1964, *MNRAS*, 128, 307
 Sersic J. L., 1968, *Atlas de Galaxias Australes*. Obs. Astron. Univ. Nacional de Cordoba, Cordoba
 Shajib A. J., et al., 2023, *A&A*, 673, A9
 Shuntov M., et al., 2025, *A&A*, 696, L14
 Skelton R. E., et al., 2014, *ApJS*, 214, 24
 Sonnenfeld A., 2024, *A&A*, 690, A325
 Sonnenfeld A., Gavazzi R., Suyu S. H., Treu T., Marshall P. J., 2013a, *ApJ*, 777, 97
 Sonnenfeld A., Treu T., Gavazzi R., Suyu S. H., Marshall P. J., Auger M. W., Nipoti C., 2013b, *ApJ*, 777, 98
 Sonnenfeld A., Treu T., Marshall P. J., Suyu S. H., Gavazzi R., Auger M. W., Nipoti C., 2015, *ApJ*, 800, 94
 Sonnenfeld A., et al., 2018, *PASJ*, 70, S29

- Sonnenfeld A., et al., 2020, *A&A*, 642, A148
 Spergel D., et al., 2015, *arXiv e-prints*, p. arXiv:1503.03757
 Tan C. Y., et al., 2024, *MNRAS*, 530, 1474
 Thuruthipilly H., Zdrozny A., Pollo A., Biesiada M., 2022, *A&A*, 664, A4
 Trenti M., Stiavelli M., 2008, *ApJ*, 676, 767
 Treu T., Koopmans L. V. E., 2002, *ApJ*, 575, 87
 Virtanen P., et al., 2020, *Nature Methods*, 17, 261
 Weaver J. R., et al., 2024, *ApJS*, 270, 7
 Westcott L., et al., 2025, *ApJ*, 983, 121
 Whitaker K. E., et al., 2019, *ApJS*, 244, 16
 Windhorst R. A., et al., 2023, *AJ*, 165, 13
 van Dokkum P., Brammer G., Wang B., Leja J., Conroy C., 2024, *Nature Astronomy*, 8, 119

APPENDIX A: INITIAL SAMPLE OF LENS CANDIDATES

Figure A1 contains the RGB composite images of the initial sample of 16 candidate lenses obtained by visual inspection over the PEARLS NEP TDF and CEERS JWST fields. The high confidence candidates, are highlighted with an orange border. Their photometric redshift measurements, where available, are listed in Table A1. Table A1 also lists the criteria that excluded a candidate from the final list of high probability lenses. If either of the photometric redshift is missing, or the photo-z measurements are incompatible with a lensing geometry, the rejection criteria is flagged as ‘photo-z’, while if the simple lens mass (SIE + external shear) or source light (single Sèrsic profile) models employed are not able to reproduce the observed configuration the rejection criteria is flagged as ‘lens model’.

This paper has been typeset from a $\text{\TeX}/\text{\LaTeX}$ file prepared by the author.



Figure A1. Initial sample of lens candidates in PEARLS NEP field and CEERS fields, shown as $10'' \times 10''$ cutouts centred on the candidate deflector. The systems highlighted with an orange border are the 4 high-confidence strong lenses with measured photometric redshifts and a lens model.

Table A1. Photometric redshift measurements for the 16 systems flagged as candidate lenses in the visual inspection process.

Name	R.A.	DEC	$z_{\text{lens}}^{\text{phot}}$	$z_{\text{source}}^{\text{phot}}$	Rejection Criteria	Comments
PEARLS172312+655014	17:23:11.93	+65:50:14.32	$0.3741^{+0.002}_{-0.002}$	$2.35^{+0.05}_{-0.15}$	-	(a)
PEARLS172239+655143	17:22:38.98	+65:51:43.16	$1.25^{+0.25}_{-0.25}$	$3.60^{+0.10}_{-0.10}$	-	(b)
PEARLS172244+655623	17:22:43.90	+65:56:22.97	$0.60^{+0.09}_{-0.11}$	$1.45^{+0.14}_{-0.21}$	-	
PEARLS172340+654936	17:23:39.60	+65:49:35.75	$[0.38^{+0.08}_{-0.10}]$	$[2.60^{+0.20}_{-0.20}]$	lens model	
PEARLS172233+654754	17:22:33.16	+65:47:53.66	$[0.57^{+0.15}_{-0.15}]$	$[2.90^{+0.14}_{-0.14}]$	lens model	(c)
PEARLS172253+654847	17:22:53.14	+65:48:47.42	$[0.55^{+0.1}_{-0.1}]$	$[0.65^{+0.1}_{-0.1}]$	photo-z	(d)
PEARLS172242+654338	17:22:42.68	+65:43:38.02	$[0.63^{+0.1}_{-0.1}]$	-	both	(e)
PEARLS172245+655442	17:22:45.26	+65:54:41.96	$[0.98^{+0.1}_{-0.1}]$	-	both	(e)
CEERS141956+525740	14:19:56.24	+52:57:40.80	-	-	both	
CEERS141957+525926	14:19:57.30	+52:59:26.22	-	-	both	
CEERS141933+525301	14:19:33.33	+52:53:00.90	$[1.13^{+0.19}_{-0.17}]$	$[1.51^{+0.15}_{-0.13}]$	lens model	(f)
CEERS141857+524542	14:18:56.75	+52:45:42.45	-	-	photo-z	(g)
CEERS141856+524528	14:18:55.60	+52:45:27.80	$[1.55^{+0.18}_{-0.18}]$	$[1.61^{+0.18}_{-0.18}]$	photo-z	(d)
CEERS141938+525126	14:19:37.53	+52:51:25.97	-	-	lens model	
CEERS142032+525823	14:20:31.80	+52:58:22.90	$0.380^{+0.005}_{-0.005}$	$0.99^{+0.05}_{-0.05}$	-	(h)
CEERS142021+525543	14:20:21.48	+52:55:43.12	$[0.73^{+0.03}_{-0.24}]$	$[4.21^{+0.14}_{-0.21}]$	lens model	

Notes. From left to right, the columns indicate the lens name, right ascension and declination, photometric redshifts of the deflector and of the background source, and the criteria that excluded the system from the high-confidence sample (either photo-z or lens modeling). The systems without both redshift measurements or with measurements listed in square brackets are not included in the final sample of high-confidence lens candidates.

Comments. (a) This deflector has spectroscopic redshift measured with Binospec at the MMT [Willmer, personal communication]. (b) This source also lies in a NIRISS pointing, and the spectral extraction (Estrada-Carpenter et al. 2024) yields redshift of $z_{\text{lens}} = 1.258 \pm 0.005$ (more details will be presented in Adams et al. 2025); (c) Both deflector and source photo-z are bimodal ($z_{\text{lens}} = 0.57$ or 1.82 , $z_{\text{source}} = 0.3$ or 2.9). Suspected arc may be part of diffraction spike (clover pattern) of galaxy bulge; (d) Source just behind foreground galaxy; (e) Starburst inside host; (f) The SED shows a 1.6 micron bump at $z=1.0$ - 1.2 not 1.5 , these may be companion/minor merger; (g) The three point images are part of diffraction spike; (h) Target in the blue module gap. This lens was also found in SL2S with spectroscopic redshifts for deflector and source, reported in the table. Our estimate of the photo-z for this galaxies has a large error due to NIRCcam blue module gap: $z_{\text{lens}}^{\text{phot}} = 0.1^{+0.4}_{-0.05}$, $z_{\text{source}}^{\text{phot}} = 0.75^{+0.63}_{-0.33}$.